Inorganic Chemistry
Cite This: Inorg. Chem. 2019, 58, 4553−4560
Article
pubs.acs.org/IC

Role of f Electrons in the Optical and Photoelectrochemical Behavior of $Ca(La_{1-x}Ce_x)_2S_4$ ($0 \leq x \leq 1$)

Paola Sotelo,[†] Melissa Orr,[†] Miguel T. Galante,[†,§] Mohammad Kabir Hossain,[†] Farinaz Firouzan,[†] Claudia Longo,[§] Attila Kormányos,[∥,⊥] Hori Sarker,[‡] Csaba Janáky,[∥,⊥] Mohammad N. Huda,[‡] Krishnan Rajeshwar,[†] and Robin T. Macaluso*[,†]

[†]Department of Chemistry and Biochemistry, The University of Texas at Arlington, Arlington, Texas 76019, United States
[‡]Department of Physics, The University of Texas at Arlington, Arlington, Texas 76019, United States
[§]Institute of Chemistry, University of Campinas—UNICAMP, 13083-970, Campinas, Brazil
[∥]Department of Physical Chemistry and Materials Science, University of Szeged, Rerrich Square 1, Szeged H-6720, Hungary
[⊥]Lendület Photoelectrochemistry Research Group, MTA-SZTE, Rerrich Square 1, Szeged H-6720, Hungary

Supporting Information

ABSTRACT: This study focuses on a solid solution series, $Ca(La_{1-x}Ce_x)_2S_4$ ($0 \leq x \leq 1$), where the f electron density is absent in $CaLa_2S_4$ and is progressively increased until it is maximized in $CaCe_2S_4$. Correspondingly, these samples, synthesized by a sealed ampule method, showed progressive variations in color ranging from gray for $CaLa_2S_4$ to orange-red for $CaCe_2S_4$. The crystal structural nuances of both the end members and three solid solutions with x = 0.25, 0.50, and 0.75 were established with the complementary use of synchrotron X-ray diffraction and neutron scattering. Interestingly, these data were consistent with a two-phase composition centered around each nominal solid solution stoichiometry. Optical characterization via diffuse reflectance spectroscopy and Tauc analyses showed a shrinking of the energy band gap (from the UV to vis range) when Ce was progressively introduced into the host $CaLa_2S_4$ structure. These data were in concert with electronic band structure calculations, using density functional theory, which showed the progressive formation of an intermediate f band when Ce was introduced intro the structure. Photoelectrochemical measurements in an aqueous redox electrolyte, as well as surface photovoltage and Kelvin probe measurements, revealed all samples to be n-type semiconductors. The valence and conduction band edge positions of the end members and the three solid solutions could be mapped, on both the redox and vacuum reference energy scales, by combining these measurements with the optical data.

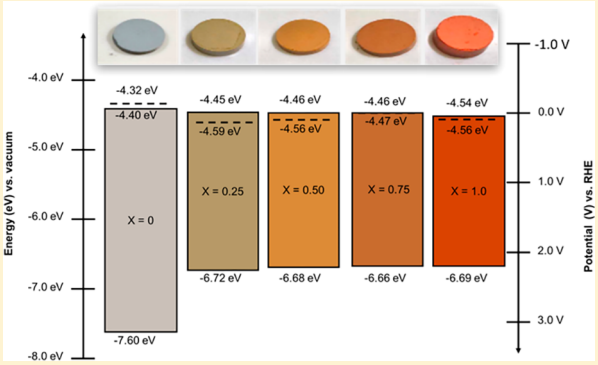

INTRODUCTION

Metal chalcogenides have long been of interest to chemists because of their applicability in diverse technologies including thermoelectrics, photovoltaics, nonlinear optics, and even superconductors and topological insulators.[1−6] The scientific community continues to explore rare-earth chalcogenides with new structures; synthetic techniques such as molten polychalcogenide fluxes and characterization of these materials using in situ diffraction (panoramic synthesis) have contributed to the fast-growing expansion of chalcogenide materials in general.[1]

Rare-earth chalcogenides are particularly interesting because of their wide array of crystal structures and physical properties.[2,3] As examples of notable discoveries of new rare-earth chalcogenides in recent years, $Ce_8Sb_2S_{15}$ exhibits a red color due to a 4f to 5d electronic transition and crystallizes in a noncentrosymmetric space group.[4] The choice of rare-earth metal can profoundly impact structure; for example, Ce_4GaSbS_9 crystallizes in a noncentrosymmetric space group, but attempts at producing a La analogue yielded a new compound, $La_2Ga_{0.33}SbS_5$, which crystallizes in a centrosymmetric space group.[5]

Quaternary rare-earth chalcogenides have also been recently found through exploratory syntheses, including Nd_7FeInS_{13} and Pr_7CoInS_{13}[6] and selenides, such as $Ba_2REGaSe_5$ and $Ba_2REInSe_5$, which are part of the larger Ba_2REMCh_5 (M = Ga, In; Ch = S, Se, or Te) family that covers four different structure types.[7] $BaLnSn_2Q_6$ (Ln = Ce, Pr, or Nd; Q = S or Se) exhibits mixed-valent Sn sites.[8] Ba_3LnInS_6 (Ln = Pr, Sm, Gd, or Yb) consists of LnS_6 distorted triangular prisms in a new structure type, and Ba_2NdGaS_5 possesses a band gap corresponding to its observed red color.[9] The chiral chalcogenide, La_4InSbS_9, contains a stereochemically active

Received: January 14, 2019
Published: March 19, 2019

DOI: 10.1021/acs.inorgchem.9b00062
Inorg. Chem. 2019, 58, 4553−4560

lone pair from Sb^{3+} and demonstrates strong potential as a nonlinear optical material in the infrared range.[10]

Rare-earth chalcogenides with the Th_3P_4-type are particularly intriguing as they can exhibit metallic to insulating behavior as well as magnetic or superconducting properties.[11] This structure can be understood by considering the structure of Ce_3S_4, which adopts the cubic Th_3P_4-type. With metal vacancies, the chemical formula can be rewritten as $Ln_{2.67}S_4$. When the vacancies are occupied by an alkaline-earth metal, $CaLn_2S_4$ (Ln = La, Ce) is the resultant stoichiometry when one-third of the Ln sites are substituted by Ca. $CaCe_2S_4$ is a red-orange compound that was eventually patented as a coating. $CaLa_2S_4$ shares the same structure, but its optical absorption edge in the UV-range and chemical stability makes it applicable as a ceramic window coating.[12]

One distinguishing feature of rare-earth chalcogenides is the localized nature of the 4f band. In CeSF, the localized nature of the Ce atom and the low dimensional crystal structure of CeSF results in an optical transition between S 3p → Ce 4f states.[13] Band structure calculations show that the Ce 4f → Ce 5d electronic transition in alkali-earth-doped-Ce_2S_3[14] is responsible for their observed red color. Additionally, the f → d electronic transitions are *intraband* in nature as opposed to the interband transitions responsible for colors in other well-known metal chalcogenide pigments, CdS and CdSe.[14] The observed red-orange color of $CaCe_2S_4$ is intrinsically caused by the presence of the rare-earth element, Ce, and hence, the presence of f electron density.

To better understand the role of f electrons in optical rare-earth based chalcogenides, we strategically chose to investigate a solid solution series, $Ca(La_{1-x}Ce_x)_2S_4$ ($0 \le x \le 1$), where the f electron density is absent in $CaLa_2S_4$ and is progressively increased until it is maximized in $CaCe_2S_4$. The effects of increasing f electron density in $Ca(La_{1-x}Ce_x)_2S_4$ ($0 \le x \le 1$) are presented below with respect to structural, optical, and photoelectrochemical behavior. When we initially synthesized compounds in this series, the colors of the samples ranged from orange-red in $CaCe_2S_4$ to green in $Ca(La_{0.75}Ce_{0.25})_2S_4$, as shown in Figure 1. This tangible progression further motivated a detailed study of structure and photoelectrochemical behavior of these solid solutions, as presented in this Article.

Figure 1. Photographs of $Ca(La_{1-x}Ce_x)_2S_4$ ($0 \le x \le 1$) samples show the color variation of x = 0, 0.25, 0.50, 0.75, and 1.0 compositions.

MATERIALS AND METHODS

Synthesis. Powder samples of $Ca(La_{1-x}Ce_x)_2S_4$ ($0 \le x \le 1$) were prepared by grinding a stoichiometric ratio of CaS, Ce_2S_3, and La_2S_3 with an agate mortar and pestle. The powders were ground and placed in tantalum foil inside a drybox filled with circulating ultrahigh purity argon. The foil and its contents were placed inside a fused silica ampule and sealed under vacuum. Ampules were heated at 7 °C/h to 1100 °C, where it dwelled for 100 h, and then cooled to 25 °C at 20 °C/min. Typical yields based on mass were ~99%. The most common impurity was identified as Ce_2O_2S.

X-ray Diffraction. High resolution X-ray powder diffraction data were collected using Beamline 11-BM at the Advanced Photon Source, Argonne National Laboratory, using an average wavelength of 0.414555 Å for $Ca(La_{0.25}Ce_{0.75})_2S_4$ and $Ca(La_{0.75}Ce_{0.25})_2S_4$ and 0.41273 Å for $Ca(La_{0.50}Ce_{0.50})_2S_4$. Discrete detectors covering an angular range from −6° to 16° in 2θ were scanned over a 2θ range of 34°, with data points collected every 0.001° in 2θ at a scan speed of 0.01°/s. Data were collected at room temperature.

The X'Pert Plus software package[15] was employed to analyze synchrotron data. A previously established structural model of $CaLn_2S_4$ (Ln = La, Ce)[16] was used as a starting model for the refinement of $CaLa_2S_4$ and $CaCe_2S_4$. Global profile refinement parameters included a scale factor, a specimen displacement parameter, and peak shape function (U, V, W).[17] The peak shape was fit using a pseudo-Voigt function,[18] and the background was manually determined. Unit cell parameters, site occupancies, and anisotropic/isotropic displacement parameters were refined.

Neutron Diffraction. Time-of-flight neutron diffraction data were collected for $Ca(La_{1-x}Ce_x)_2S_4$ (x = 0.25, 0.5, 0.75) using the POWGEN powder diffractometer at Oak Ridge National Laboratory. Time-of-flight data were collected at 300 K using a 60 Hz frequency at with a frame at a center wavelength of 1.066 Å, covering a d-spacing range 0.2−5.0 Å. The collected neutron diffraction data were analyzed by a full pattern Rietveld refinement, using the JANA software package.[19] The convolution pseudo-Voigt function with back-to-back exponential functions was used as a peak shape function.

Electron Microscopy. Electron dispersive spectroscopy measurements were performed with a Hitachi S-3000N FE scanning electron microscope. Polycrystalline samples were mounted on carbon tape and placed into an evacuated chamber. The electron beam energy was 20 kV. Scans were collected from multiple spots on several crystals. Energy-dispersive X-ray spectroscopy (EDS) analyses indicated that elemental composition was in good agreement with expected stoichiometric ratios. These results can be found in Supporting Information.

Diffuse Reflectance Spectroscopy. Optical band gaps of $Ca(La_{1-x}Ce_x)_2S_4$ ($0 \le x \le 1$) were determined by diffuse reflectance spectroscopy (DRS) coupled with Tauc analyses.[20,21] DRS data were collected from 300 to 1000 nm using a PerkinElmer Lambda 35 spectrophotometer equipped with an integrating sphere accessory. The absorption spectrum was calculated from the reflection spectrum via the Kubelka−Munk function $\alpha/S = (1 - R)^2/2R$, where α is the absorption coefficient, S is the scattering coefficient, and R is the reflectance.[20]

Photoelectrochemistry. Films of $Ca(La_xCe_{1-x})_2S_4$ were prepared by depositing a suspension of $Ca(La_xCe_{1-x})_2S_4$, polyethylene glycol (PEG, MW 20 000), and water in a 1:1:5 ratio by mass. Suspensions were deposited on a 1.0 cm^2 Ti substrate. Prior to film deposition, the Ti substrates were cut into 3.0 × 1.0 cm^2 pieces and chemically etched in 36% HCl to remove organic contaminants.

To improve adhesion of the sulfide compound to the Ti substrate, films were dried in ambient temperature and further annealed in a box furnace at 350 °C for 30 min and subsequently at 450 °C for 30 min.

Electrochemical measurements were carried out using a three-electrode cell with Pt foil as a counterelectrode and Ag/AgCl/KCl 4 M as reference electrode in a standard single-compartment electrochemical cell and a CH Instruments potentiostat (model CHI720C). Additionally, 0.1 M Na_2SO_4 was used as a supporting electrode, with 0.1 M Na_2SO_3 added as a hole scavenger. The electrolyte solutions were purged with ultrapure N_2 for 15 min prior to the photovoltammetry measurements.

Photovoltammetry measurements were recorded at a low scan rate of 5 mV s^{-1} in which a sweep potential was applied from −0.6 V up to +1.0 V. A manual chopper was used to create a 5 s interval dark/illuminated cycles. Throughout the measurements, a radiation source (400 W Xe lamp) was kept at a fixed distance from the cell (20 cm). The nominal incident photon flux at the location of the photoelectrode was 300 mW/cm^2, measured on a Newport model 70260 Radiant Power/Energy meter combined with a probe (Newport, 70268).

Kelvin Probe Measurements and Surface Photovoltage Spectroscopy. Measurements were performed using a KP Technology APS04 instrument.[21] First, the Fermi level of the gold-

DOI: 10.1021/acs.inorgchem.9b00062
Inorg. Chem. 2019, 58, 4553−4560

alloy-coated tip was determined by measuring the Fermi level of a Ag target ($E_{Fermi,Au\text{-}tip}$ = −4.61 eV). Thin film samples were studied as in the case of the photoelectrochemical experiments. A 2 mm diameter gold-alloy-coated tip was vibrated above the sample surface at a fixed height (∼1 mm) and amplitude (0.2 mm), with a constant frequency (70 Hz). The contact potential difference (CPD) was measured between the sample and the Kelvin probe tip after electric equilibrium was reached. Surface photovoltage (SPV) spectroscopy was performed under ambient conditions. The gold-coated Kelvin probe tip served as the reference electrode. The samples were illuminated with monochromatic light (Fiber-Lite DC950 150W quartz halogen lamp, coupled to a monochromator).

Computational Methodology. The present calculations were performed on the framework of spin polarized density functional theory (DFT)[22,23] as implemented in the Vienna ab initio simulation package (VASP).[24,25] The exchange and correlation were treated via the generalized gradient approximation (GGA) formalized by Perdew−Burke−Ernzerhof (PBE).[26] The projector augmented plane wave (PAW) method[6] was used to describe the interaction between the core and valence electrons. The electronic basis set was expanded in terms of plane wave, and a plane wave kinetic energy cutoff, E_{cut} of 600 eV, was used throughout the calculation. VASP supplied standard PAW potentials were applied for La, Ce, and S atoms and the Ca_sv version of PAW potential for Ca atom for geometric optimization and electronic structure calculations.

The Monkhorst−Pack (MP) scheme was used to generate the k-points mesh within the first Brillouin zone. In this present calculation, a 3 × 3 × 3 k-point mesh was used for geometric optimization which gave a well-converged calculation. During the geometrical optimization, the atoms in the unit cell were fully relaxed until the residual forces among the constituent atoms became less than 0.01 eV $Å^{-1}$. Methfessel−Paxton smearing was also used with a width of 0.002 eV for geometric optimization and the tetrahedron method with Blöch corrections for the density of state (DOS) calculation. Apart from using the DFT method to calculate the lattice parameters, the rotationally invariant DFT+U method[7] was also deployed. For DFT +U calculation of lattice parameters, U values of 5 eV were used for the La d state and the Ce f state simultaneously.

RESULTS AND DISCUSSION

Crystal Structure. The series, $Ca(La_{1-x}Ce_x)_2S_4$, adopts the cubic Th_3P_4 structure type, which has been described previously for the end members, x = 0 and 1.[27] Neutron diffraction was employed as La and Ce cannot be easily distinguished using X-ray sources. Indeed, neutron coherent scattering cross sections of the most abundant isotopes of La, Ce, and Ca are ∼8.24, 4.84, and 4.20 fm, respectively; hence, La can be easily distinguished from the other elements present.[28] The neutron diffraction patterns, shown in Figure 2, show that the Th_3P_4 structure type is maintained throughout the solid solution, $Ca(La_{1-x}Ce_x)_2S_4$. Furthermore, refined unit cell dimensions obey Vegard's law with cell parameters of 8.6391(4), 8.6579(4), and 8.6717(3) Å for members with x = 0.75, 0.50, and 0.25, respectively.

Splitting of diffraction peaks was immediately observed upon analyzing synchrotron data (Figure 3), which has a higher resolution than neutron data. Such peak splitting is typically indicative of multiphase samples. It is important to note that refined lattice parameters do not correspond to end members, and *hence, the synthesized materials are not simply proportional mixtures of* $CaLa_2S_4$ *and* $CaCe_2S_4$. Rather, the La and Ce mixing is chemically intrinsic for each sample. For each nominal composition, at least two phases with two unique sets of unit cell parameters can be refined using synchrotron diffraction data. This two-phase model yielded reasonable statistical fits with goodness-of-fit between 1 and 2.

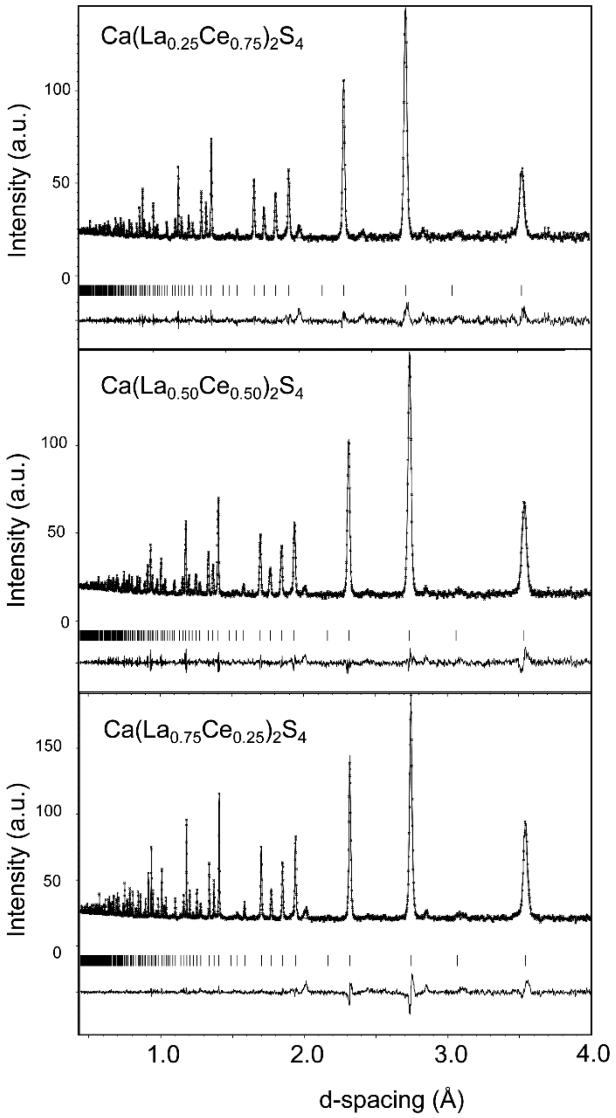

Figure 2. Rietveld refinements of neutron diffraction data for $Ca(La_{1-x}Ce_x)_2S_4$, x = 0.25, 0.50, 0.75. Black tick marks and red lines represent experimental data and structural model, respectively. Calculated peaks are shown as vertical dashed lines, and the difference plot is shown as a black line at the bottom.

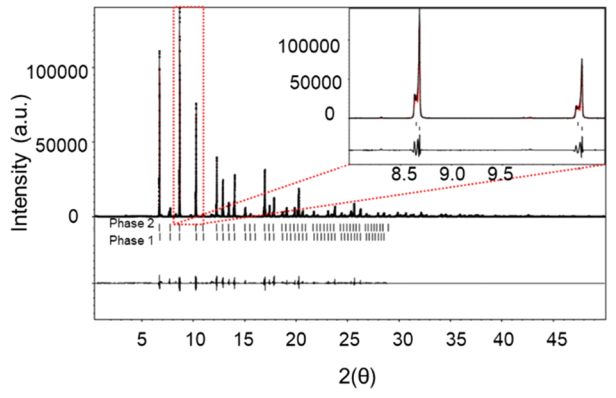

Figure 3. Refinement of synchrotron diffraction data for $Ca(La_{0.25}Ce_{0.75})_2S_4$. Inset: Data between 2θ are enlarged for ease of viewing peak splitting.

DOI: 10.1021/acs.inorgchem.9b00062
Inorg. Chem. 2019, 58, 4553−4560

For the x = 0.25, 0.50, and 0.75 samples, two distinct compositional domains could be observed and assigned to a specific set of diffraction peaks. Diffraction data reveal one major and one minor domain for $Ca(La_{0.25}Ce_{0.75})_2S_4$ and $Ca(La_{0.75}Ce_{0.25})_2S_4$, whereas two quantitatively identical crystallographic domains are observed for $Ca(La_{0.5}Ce_{0.5})_2S_4$. Figures 3 and 4 present representative collected diffraction data as well as the refined cell parameters, respectively.

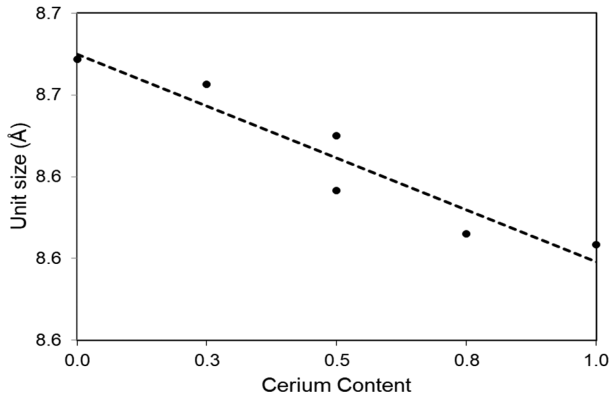

Figure 4. Cell parameters for $Ca(La_{1-x}Ce_x)_2S_4$ as a function of cerium content for x = 0, 0.25, 0.50, 0.75, 1.0, values based on refinement of synchrotron data. For x = 0.25 and 0.75, only the major phase is included. For x = 0.50, both phases, equally intense, are included. Additional information is provided in Supporting Information (Tables S1 and S2).

Optical Properties. Diffuse reflectance spectroscopy (DRS) was utilized to map progressive changes in the optical properties of $CaLa_2S_4$ as Ce was introduced into the structural framework. Figure 5a contains the DRS data; the parent transition in the lanthanum compound centered ca. 400 nm shifts to longer wavelengths (~500−550 nm) as Ce is introduced. Tauc plots were constructed from Kunbelka−Munk transformation of the DRS data; these plots for $Ca(La_{1-x}Ce_x)_2S_4$ (Figure 5b) clearly show that the optical band gap is dependent upon Ce substitution, x. Although the shift from 2.15 eV in $CaCe_2S_4$ to 2.27 eV in $Ca(La_{0.25}Ce_{0.75})_2S_4$ is small, these values correspond to the visibly different colors of the corresponding materials (Figure 1).

To further clarify whether the x = 0.25−0.75 samples were simply physical mixtures of $CaCe_2S_4$ and $CaLa_2S_4$ or if the Ce and La in the materials were truly and chemically mixed at the atomic level, equal amounts of $CaCe_2S_4$ and $CaLa_2S_4$ end members were ground and pressed into a pellet. This physical mixture exhibited different optical behavior as evidenced in the DRS data in Figure 5a. The Tauc plot shows that the band gap of the $Ca(La_{0.50}Ce_{0.50})_2S_4$ solid solution measures 2.39 eV (Figure 5b) whereas the band gap of the physical mixture (labeled as $CaLa_2S_4$ + $CaCe_2S_4$ − PM) clearly exhibits two peaks corresponding to 2.32 and 3.20 eV which are similar to the band gaps of $CaCe_2S_4$ and $CaLa_2S_4$, respectively (Figure 5a).

DFT Results. Table S1 lists the crystallographic lattice parameters of the geometrically relaxed structures; for comparison, both the DFT and DFT+U lattice parameters are presented. Figure 6 shows the band structure and partial density of states of $CaLa_2S_4$. The calculated band gap is 2.06 eV and is direct. The main contribution to the valence band is from the S p state, and the dominant contribution to the

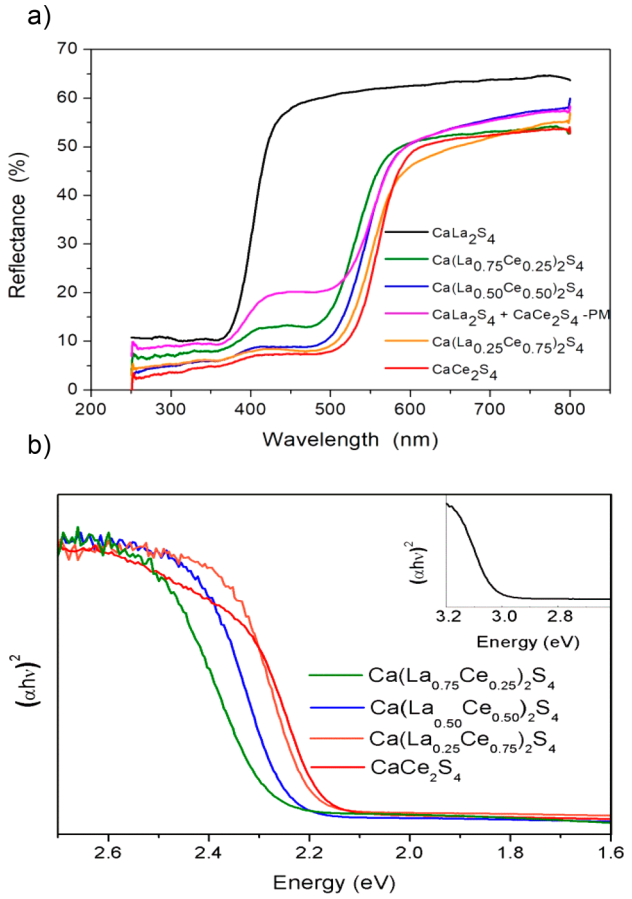

Figure 5. (a) Diffuse reflectance data and (b) Tauc plots for $Ca(La_{1-x}Ce_x)_2S_4$ (x = 0.25, 0.50, 0.75, and 1.0) powder. The inset in part a contains the Tauc plot for $CaLa_2S_4$.

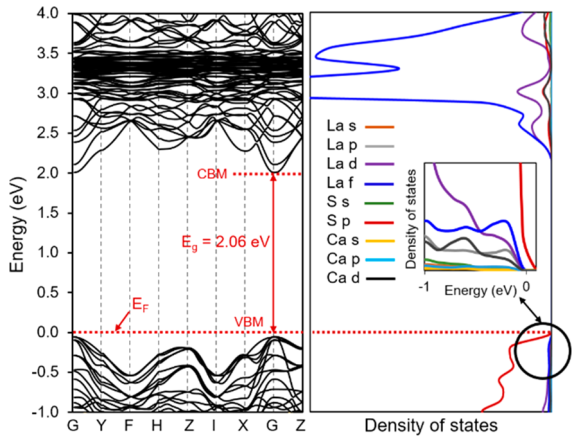

Figure 6. Band structure and partial density of states for $CaLa_2S_4$. The contribution of different electronic states near the Fermi level is shown in the inset. VBM and CBM correspond to valence band minimum and conduction band minimum, respectively.

conduction band minima is from La f states. There is hybridization between La f and d states at the bottom of the conduction band. Thus, electronic transitions in $CaLa_2S_4$ will originate from the occupied S p state to the unoccupied La f state. Just above the conduction band minima, there are localized bands created by La f states. The localization of La f states is indicated as a sharp peak in the partial density of states plot.

DOI: 10.1021/acs.inorgchem.9b00062
Inorg. Chem. 2019, 58, 4553−4560

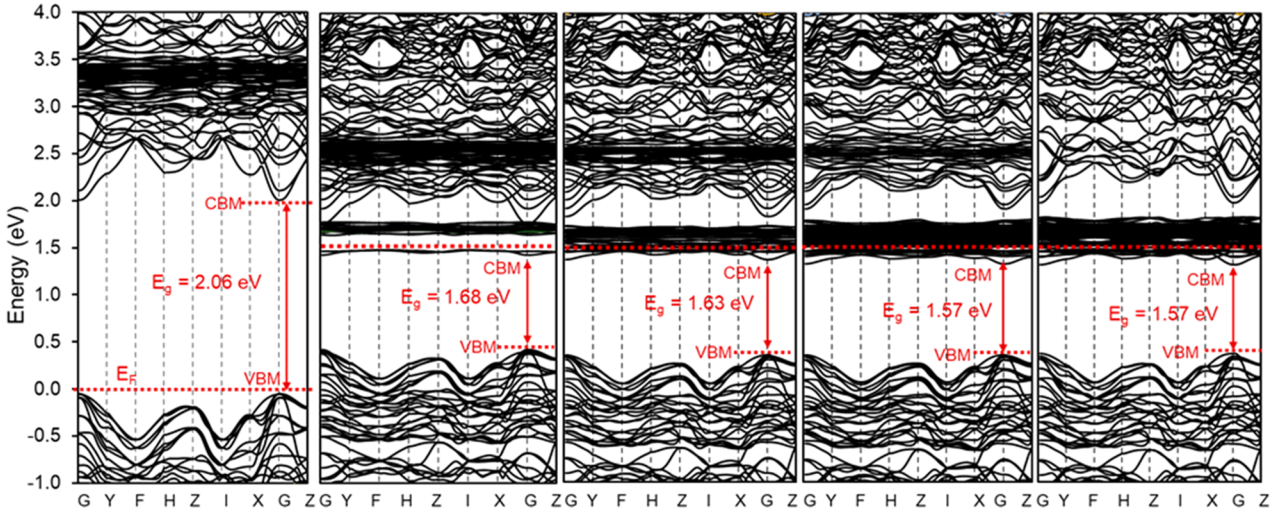

Figure 7. Band structure and partial density of states for x = 0.0, 0.25, 0.50, 0.75, and 1.0 of $Ca(La_{1-x}Ce_x)_2S_4$.

Figure 7 presents the DFT-derived electronic band structures for the progression from x = 0, 0.25, 0.50, 0.75 and culminating in the Ce compound, $CaCe_2S_4$. The left-most frame is reproduced from Figure 6, simply for comparison. The valence band maxima clearly remain unchanged from $CaLa_2S_4$. The Ce f states become the main contribution to the conduction band minima as this element is introduced into the $CaLa_2S_4$ structure. The Ce f states create a localized band at the bottom of the conduction band. The localization is indicated as a sharp peak in the partial density of states plot (not shown). Due to the introduction of Ce within $CaLa_2S_4$, the Fermi level shifts to the conduction band minima, consistent with n-type semiconductor behavior (see below). Cerium incorporation also creates occupied states at the bottom of the conduction band, and the number of occupied states at the conduction band minima increases as the Ce level increases.

Optical transitions in Ce-containing $Ca(La_{1-x}Ce_x)_2S_4$ will occur from occupied S p states to unoccupied Ce f states. Accordingly, the shifts in the transitions seen in the DRS data (Figure 5a) in $Ca(La_{1-x}Ce_x)_2S_4$ for x = 0.25, x = 0.5, x = 0.75, and x = 1.0 are 1.68, 1.63, 1.57, and 1.52 eV, respectively, and the nature of the band gap is direct. These values are lower than those derived from DRS data (see above) and also from other measurements (see below). However, such a discrepancy is not uncommon between DFT and experimentally derived band gap energies. What is important for the absolute DFT-derived values is the trend with x. Importantly, both theory and experiment yield similar trends with composition.

Kelvin Probe and Surface Photovoltage Spectroscopy Results. To determine the Fermi levels of $Ca(La_{1-x}Ce_x)_2S_4$, Kelvin probe measurements were performed (see Figure S1 for the CPD data).[22] The Fermi levels (E_F's) fall close to the E_{CB} values of all four compounds (Table 1), which is characteristic for n-type semiconductors.[23] The E_F of $CaLa_2S_4$ is less negative, compared to the alloyed samples, which are in the same range. To better understand the optoelectronic properties, surface photovoltage (SPV) measurements were also performed. SPV is a sensitive tool to probe the wavelength dependence of light-driven charge separation; thus, it can deliver information about the band gap, majority carrier type, and defect states.[24,25] All samples gave negative photovoltage values (Figure 8), indicating that they behave as n-type semiconductors.[24,26,29] Band gap values were calculated from the onset of the SPV spectra (Table 1). These values are slightly smaller, compared to those obtained from DRS measurements. The reason behind this difference is that SPV is inherently much more sensitive to *sub-band-gap* effects (such as the Franz–Keldysh effect and the photoassisted charge transfer between shallow states extending from the band gap "tail states").[24] After reaching a maximum, the SP signal decreases at the lower wavelengths (except in the case of the $CaLa_2S_4$ sample where this maximum cannot be measured due to the wider band gap) since the top layer absorbs all the light, which no longer can penetrate to the bottom of the films to generate photovoltage.[25]

Table 1. Band Gap (E_{BG}) and Fermi Level (E_F) Values of $Ca(La_{1-x}Ce_x)_2S_4$ (x = 0.25, 0.5, 0.75, and 1.0) from DRS, KP, and SPV Measurements

sample	EBG, DRS (eV)	EBG, SPS (eV)	E_F (eV)
$CaLa_2S_4$	3.20	2.76	−4.31
$Ca(La_{0.75}Ce_{0.25})_2S_4$	2.27	2.10	−4.47
$Ca(La_{0.50}Ce_{0.50})_2S_4$	2.22	2.29	−4.56
$Ca(La_{0.25}Ce_{0.75})_2S_4$	2.20	2.13	−4.59
$CaCe_2S_4$	2.15	2.11	−4.56

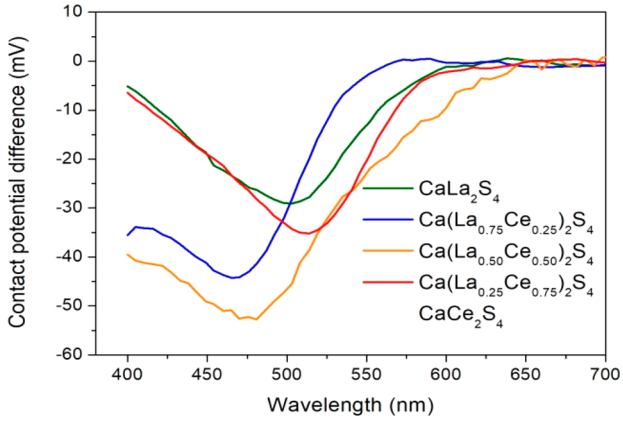

Figure 8. Surface photovoltage spectra recorded for $Ca(La_{1-x}Ce_x)_2S_4$ (x = 0.25, 0.5, 0.75, and 1.0) thin films on Ti substrate.

DOI: 10.1021/acs.inorgchem.9b00062
Inorg. Chem. 2019, 58, 4553−4560

Photoelectrochemical Behavior. The photoelectrochemical properties of $Ca(La_{1-x}Ce_x)_2S_4$ thin film electrodes were evaluated by means of linear sweep voltammetry under intermittent light incidence and compared to those of the two end members. As shown in Figure 9, anodic photocurrent was

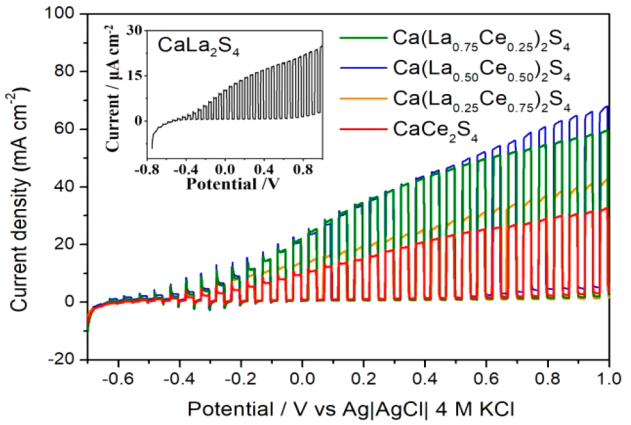

Figure 9. Photocurrent measurements under intermittent light incidence of thin film electrodes polarized at $E > E_{eq}$, immersed in aqueous 0.1 M Na_2SO_4 solution containing 0.1 M Na_2SO_3 as hole scavenger. Pt wire was the counterelectrode.

observed for all samples when polarized at $E > E_{eq}$ in the presence of Na_2SO_3 as hole scavenger in solution, consistent with n-type semiconductor behavior (see above). While the lowest current density was observed for $CaLa_2S_4$ (inset in Figure 9), higher current densities were measured for cerium-containing samples. As Ce is progressively substituted for La, higher current densities were measured. The highest current density (at a fixed potential, 1.23 V vs RHE) was observed for $x = 0.50$ (Figure 10).

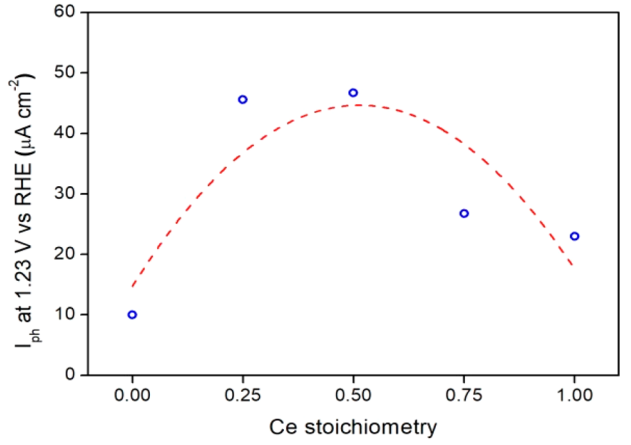

Figure 10. Relationship between photocurrent at 1.23 V vs RHE and cerium stoichiometry of $Ca(La_xCe_{1-x})_2S_4$ compounds. The dashed line was simply drawn as a guide to the data trend.

While incorporation of Ce was beneficial up to a point, higher amounts were clearly deleterious, and in fact, $CaLa_2S_4$ exhibited inferior activity relative to the other samples in Figures 8 and 10. Clearly, other factors (bulk carrier transport, surface electrocatalytic activity) must play a role here; a delineation of these will require further study beyond the scope of the present one. It is also tempting to attribute the localized nature of f electronic states in limiting carrier transport, and these states are maximally expressed in $CaLa_2S_4$ relative to the other samples. In other words, the shrinking of the energy band gap exerts a beneficial effect as Ce is first introduced. Progressive incorporation results in the manifestation of f band limitations arising from their localized nature.

Butler–Gärtner plots[23] were constructed from the photoelectrochemical data and flat-band potentials were extracted from these curves (Figure S2). Band positions can be estimated by combining this information with optical band gaps (Figure 11). Interestingly, both optical band gaps and

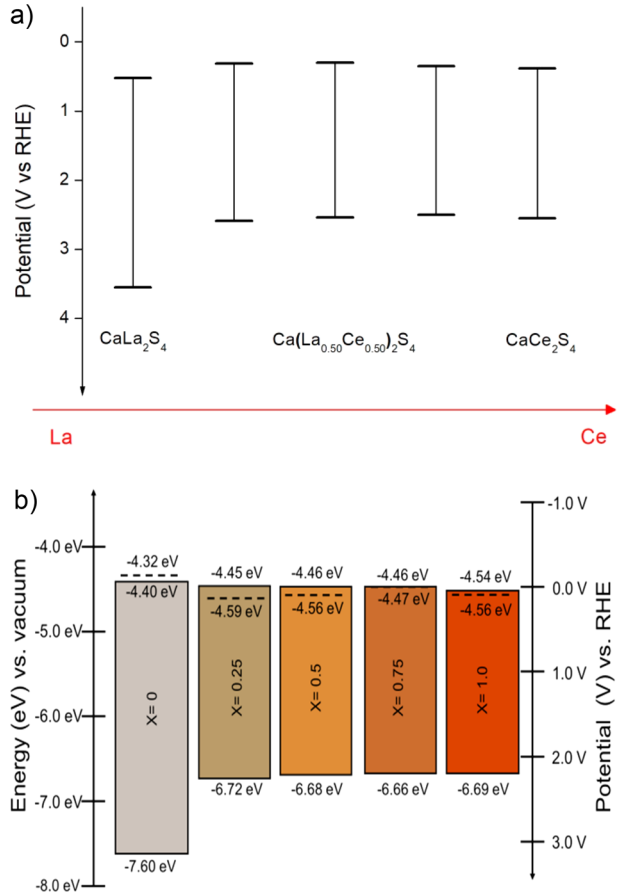

Figure 11. Band edge positions of $Ca(La_{1-x}Ce_x)_2S_4$ obtained by combining (a) flat-band potentials and optical band gaps, and (b) Kelvin probe and photoelectrochemical data.

band positions are similar for all cerium-containing samples. Finally, Figure 11b combines the information derived from the Kelvin probe and photoelectrochemical measurements for mapping the band edge locations as a function of Ce content in $Ca(La_{1-x}Ce_x)_2S_4$. This energy band diagram is shown both on the vacuum and electrochemical (i.e., RHE) reference scales.

CONCLUSIONS

The new data presented here on the two end members and three solid solutions in the series, $Ca(La_{1-x}Ce_x)_2S_4$, demonstrate an effective structural framework and chemical architecture to explore the optoelectronic role of adding f electrons. Clearly, the effect was striking on the first incorporation as exemplified by the $x = 0.25$ sample. The valence band edge immediately shifted upward resulting in a shrinking of the energy band gap from the UV range to the

DOI: 10.1021/acs.inorgchem.9b00062
Inorg. Chem. 2019, 58, 4553–4560

visible. Subsequent incorporation of Ce resulted in incremental (rather than drastic) changes in the optoelectronic behavior and electronic band structure. The photoelectrochemical data (including SPV and Kelvin probe measurements) revealed all samples to be n-type semiconductors regardless of the chemical composition. The location of the conduction band edge was relatively insensitive to the compound stoichiometry. However, the measured photocurrents in a redox electrolyte did vary with compound stoichiometry, peaking at a Ce level of $x = 0.50$.

■ ASSOCIATED CONTENT

Supporting Information

The Supporting Information is available free of charge on the ACS Publications website at DOI: 10.1021/acs.inorgchem.9b00062.

Crystal structure data and phase analyses (cf., Figure 4), electron probe microanalyses, and photoelectrochemical data for $Ca(La_{1-x}Ce_x)_2S_4$ solid solutions and end members (PDF)

■ AUTHOR INFORMATION

Corresponding Author

*E-mail: robin.macaluso@uta.edu.

ORCID

Csaba Janáky: 0000-0001-5965-5173
Mohammad N. Huda: 0000-0002-2655-498X
Krishnan Rajeshwar: 0000-0003-4917-7790
Robin T. Macaluso: 0000-0002-0021-0775

Author Contributions

The manuscript was written through contributions of all authors. All authors have given approval to the final version of the manuscript.

Notes

The authors declare no competing financial interest.

■ ACKNOWLEDGMENTS

We acknowledge O. Gourdon for many useful discussions. R.T.M. and P.S. acknowledge NSF CAREER Award 1541230 and ACS PRF New Directions Award. C.L. and M.T.G. gratefully acknowledge the CAPES−PDSE program for financial support (88881.131530/2016-01). M.N.H. was supported by National Science Foundation Award No. DMR-1609811. We gratefully acknowledge the computations time awarded by Texas Advanced Computing Center (TACC). Use of the Advanced Photon Source at Argonne National Laboratory was supported by the U. S. Department of Energy, Office of Science, Office of Basic Energy Sciences, under Contract No. DE-AC02-06CH11357. A portion of this research used resources at the Spallation Neutron Source, a DOE Office of Science User Facility operated by the Oak Ridge National Laboratory.

■ REFERENCES

(1) Kanatzidis, M. G. Discovery-Synthesis, Design, and Prediction of Chalcogenide Phases. *Inorg. Chem.* **2017**, *56*, 3158−3173.

(2) Flahaut, J. *Handbook on the Physics and Chemistry of Rare Earths*; Elsevier: New York, 1979; Vol. *4*.

(3) Cotton, S. *Lanthanide and Actinides*; Oxford University Press: New York, 1991.

(4) Zhao, H.-J.; Zhong, X.-A. Synthesis, Crystal Structure, and Optical Properties of the Noncentrosymmetric Sulfide $Ce_8Sb_2S_{15}$. *J. Solid State Chem.* **2017**, *251*, 65−69.

(5) Zhao, H.-J. Centrosymmetry vs Noncentrosymmetry in $La_2Ga_{0.33}SbS_5$ and Ce_4GaSbS_9 Based on the Interesting Size Effects of Lanthanides: Syntheses, Crystal Structures, and Optical properties. *J. Solid State Chem.* **2016**, *237*, 99−104.

(6) Iyer, A. K.; Yin, W.; Stoyko, S. S.; Rudyk, B. W.; Mar, A. Quaternary Rare-Earth Sulfides Nd_7FeInS_{13} and Pr_7CoInS_{13}. *J. Solid State Chem.* **2017**, *251*, 50−54.

(7) Yin, W.; Zhang, D.; Zhou, M.; Iyer, A. K.; Pöhls, J.-H.; Yao, J.; Mar, A. Quaternary Rare-Earth Selenides $Ba_2REGaSe_5$ and $Ba_2REInSe_5$. *J. Solid State Chem.* **2018**, *265*, 167−175.

(8) Feng, K.; Zhang, X.; Yin, W.; Shi, Y.; Yao, J.; Wu, Y. New Quaternary Rare-Earth Chalcogenides $BaLnSn_2Q_6$ (Ln = Ce, Pr, Nd, Q = S; Ln = Ce, Q = Se): Synthesis, Structure, and Magnetic Properties. *Inorg. Chem.* **2014**, *53*, 2248−2253.

(9) Feng, K.; Shi, Y.; Yin, W.; Wang, W.; Yao, J.; Wu, Y. Ba_3LnInS_6 (Ln = Pr, Sm, Gd, Yb) and Ba_2LnGaS_5 (Ln = Pr, Nd): Syntheses, Structures, and Magnetic and Optical Properties. *Inorg. Chem.* **2012**, *51*, 11144−11149.

(10) Zhao, H.-J.; Zhang, Y.-F.; Chen, L. Strong Kleinman-Forbidden Second Harmonic Generation in Chiral Sulfide: La_4InSbS_9. *J. Am. Chem. Soc.* **2012**, *134*, 1993−1995.

(11) Holtzberg, F.; Methfessel, S. Rare-earth Compounds with the Th_3P_4-Type Structure. *J. Appl. Phys.* **1966**, *37*, 1433−1435.

(12) White, W. B.; Chess, D.; Chess, C. A.; Biggers, J. V. $CaLa_2S_4$ Ceramic Window Materials for the 8 to 14 mm Region. *Proc. SPIE* **1981**, 38−43.

(13) Tomczak, J. M.; Pourovskii, L. V.; Vaugier, L.; Georges, A.; Biermann, S. Rare-Earth vs. Heavy Metal Pigments and their Colors from First Principles. *Proc. Natl. Acad. Sci. U. S. A.* **2013**, *110*, 904−907.

(14) Perrin, M. A.; Wimmer, E. Color of Pure and Alkali-Doped Cerium Sulfide: A Local-Density-Functional Study. *Phys. Rev. B: Condens. Matter Mater. Phys.* **1996**, *54*, 2428−2435.

(15) Degen, T.; Sadki, M.; Bron, E.; Konig, U.; Nenert, G. The HighScore Suite. *Powder Diffr.* **2014**, *29*, S13−S18.

(16) Flahaut, J.; Domange, L.; Patrie, M. Combinasions Formées par les sulfures des Éléments du Group des Terres Rares. 5. vue d'Ensemble sur les Systèmes formes part le Sulfure d'Yttrium avec les Sulfures des Éléments Divalents. *Bull. Soc. Chim. Fr.* **1962**, *35*, 159.

(17) Caglioti, G.; Paoletti, A.; Ricci, F. P. Choice of Collimators for a Crystal Spectrometer for Neutron Diffraction. *Nucl. Instrum.* **1958**, *3*, 223−228.

(18) David, W. I. F. Powder Diffraction Peak Shapes - Parameterization of the Pseudo-Voigt as a Voigt Function. *J. Appl. Crystallogr.* **1986**, *19*, 63−64.

(19) Petricek, V.; Dusek, M.; Palatinus, L. Crystallographic Computing System JANA2006: General Features. *Z. Kristallogr. - Cryst. Mater.* **2014**, *229*, 345−352.

(20) Murphy, A. B. Band-gap Determination from Diffuse Reflectance Measurements of semiconductor Films, and application to Photoelectrochemical Water-Splitting. *Sol. Energy Mater. Sol. Cells* **2007**, *91*, 1326−1337.

(21) Ohtani, B. Photocatalysis A to Z—What We Know and What We Do Not Know in a Scientific Sense. *J. Photochem. Photobiol., C* **2010**, *11*, 157−178.

(22) Baikie, I. D.; Grain, A. C.; Sutherland, J.; Law, J. Ambient Pressure Photoemission Spectroscopy of Metal Surfaces. *Appl. Surf. Sci.* **2014**, *323*, 45−53.

(23) Rajeshwar, K. *Electron Transfer in Chemistry*; Wiley-VCH: New York, 2001.

(24) Kronik, L.; Shapira, Y. Surface Photovoltage Spectroscopy of Semiconductor Structures: at the Crossroads of Physics, Chemistry and Electrical Engineering. *Surf. Interface Anal.* **2001**, *31*, 954−965.

(25) Wu, P.; Wang, J. R.; Zhao, J.; Guo, L. J.; Osterloh, F. E. Structure Defects in g-C_3N_4Limit Visible Light Driven Hydrogen

DOI: 10.1021/acs.inorgchem.9b00062
Inorg. Chem. 2019, 58, 4553−4560

Evolution and Photovoltage. *J. Mater. Chem. A* **2014**, *2*, 20338−20344.
(26) Zhao, J.; Osterloh, F. E. Photochemical Charge Separation in Nanocrystal Photocatalyst Films: Insights from Surface Photovoltage Spectroscopy. *J. Phys. Chem. Lett.* **2014**, *5*, 782−786.
(27) Sotelo, P.; Orr, M.; Galante, M. T.; Hossain, M. K.; Firouzan, F.; Vali, A.; Li, J.; Subramanian, M.; Longo, C.; Rajeshwar, K.; Macaluso, R. T. Ternary Rare Earth Sulfide $CaCe_2S_4$: Synthesis and Characterization of Stability, Structure, and Photoelectrochemical Properties in Aqueous Media. *J. Solid State Chem.* **2018**, *262*, 149−155.
(28) Langevin, I. L. *Neutron Data Booklet*; Old City Publishing Group, 2003.
(29) Kwolek, P.; Szacilowski, K. Photoelectrochemistry of n-Type Bismuth Oxyiodide. *Electrochim. Acta* **2013**, *104*, 448−453.

DOI: 10.1021/acs.inorgchem.9b00062
Inorg. Chem. 2019, 58, 4553−4560